Astronomy Reports, Vol. 45, No. 5, 2001, pp. 395–408. Translated from Astronomicheskiĭ Zhurnal, Vol. 78, No. 5, 2001, pp. 459–473.

Measurement of the Turbulence in the Free Atmosphere above Mt. Maĭdanak

V. G. Kornilov and A. A. Tokovinin

Sternberg Astronomical Institute, Universitetskiĭ pr. 13, Moscow, 119899 Russia

Received February 10, 2000

Abstract—Stellar scintillations were measured at Mt. Maĭdanak during 42 nights in 1998–1999 in order to estimate the contribution of the free atmosphere to the seeing. The atmosphere above 1–2 km provides a median seeing of 0.″39, which is about one-third of the total seeing (0.″70). The characteristic altitudes of turbulent layers are from 3 to 11 km above the summit, and the appearance of layers at altitudes of 3–4 km is accompanied by a degradation of the free-atmosphere seeing. The median isoplanatic angle is $\theta_0 = 2.''30$ ($\lambda = 500$ nm, at the zenith). This is the first time that such data have been obtained for Maĭdanak.

The instruments used for these measurements—a modified four-channel photometer and a prototype of a double-aperture scintillation sensor—are described in detail. The data reduction was based on accurate corrections for photon-counting statistics and the use of theoretical weighting functions relating scintillation indices to the altitudes and intensities of turbulent layers. Simultaneous or quasi-simultaneous measurements of scintillation indices using apertures of different sizes having significantly different weighting functions enable estimation of the altitude and intensity of the equivalent turbulent layer. Despite the simplicity of this one-layer model, it provides fairly robust estimates of the integrated parameters of the real free atmosphere. © *2001 MAIK "Nauka/Interperiodica".*

1. INTRODUCTION

Studies of the optical parameters of the atmosphere have gained special importance in the context of the recent vigorous progress in the development of techniques for astronomical observations with high angular resolution, such as adaptive optics and interferometry. In addition to traditional seeing measurements, knowledge of the outer turbulence scale [1], the vertical profile of the turbulence, and the wind-velocity profile is required. These additional parameters of the atmosphere have begun to be measured at observatories with better-than-average seeing.

Mt. Maĭdanak in the Uzbekistan Republic (2600 m above sea level) provides an example of such an observatory site. Basic information about this site and results of previous astro-climatic studies can be found, for example, in [2]. A new stage in the study of the astroclimate at Mt. Maĭdanak began when a differential blurring monitor was mounted, and a continuous set of seeing measurements was obtained over more than a year [3]. The median seeing (0.″70) at Mt. Maĭdanak proved to be competitive with that at Serro Paranal in Chile (0.″66 [4]) or Rogue de los Muchachos in the Canary Islands (0.″64 [5]). It is natural that interest in the site was expressed by the European Southern Observatory, which organized a campaign to measure the seeing, outer turbulence scale, and other parameters in 1998. The measurements were carried out using the ESO Differential Image Motion Monitor (DIMM) [3] and the GSM instrument developed at the University of Nice [1, 6]. During the program, we measured stellar scintillations using apertures with various shapes, in order to obtain supplementary data on the properties of the atmospheric turbulence.

Here, we describe a technique for studying turbulence in the free atmosphere based on stellar-scintillation measurements and some of the results obtained. In particular, we present estimates for the characteristic altitudes and integrated intensities of turbulent layers, which, together with other data, provide tentative estimates for the relative contribution of the free atmosphere to the total seeing. Statistical data on the isoplanatic angle, which determines the field of view of an adaptive telescope, have been obtained for Maĭdanak for the first time.

2. THEORY

Turbulence in the upper layers of the atmosphere can be studied using measurements of stellar scintillations. For example, the vertical profile of the structure coefficient of the refraction index $C_n^2(h)$ can be determined from scintillations of binary stars using SCIDAR [7]. Given this profile, it is easy to derive the total contribution of the free atmosphere:

$$E_f = \int C_n^2(h)dh, \quad (1)$$

where the integration limits for the altitude are from about 1 km to the maximum altitude of the turbulence,

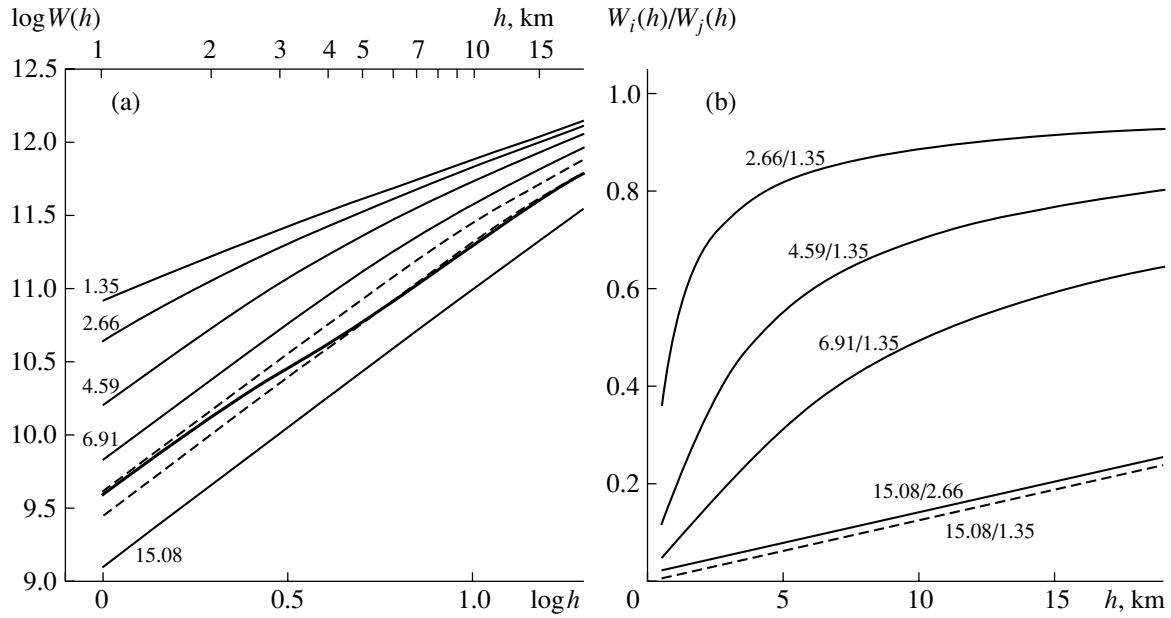

Fig. 1. (a) Weighting functions $W(h)$ for the set of entrance apertures used. The thick curve denotes the weighting function for the "isoplanatic" aperture and the dashed curve denotes that for apertures 5 and 6, which were used only in the summer of 1998. The diameters of the other apertures in cm are indicated. (b) Ratios of weighting functions for some pairs of apertures as a function of altitude h. The same functions can be understood as ratios of corresponding indices in a model with a single turbulent layer.

which is around 20 km. Comparison of E_f and the integral over the entire depth of the atmosphere $E = E_f + E_b$ provides quantitative estimates for the contributions to the total distortion of images from the free atmosphere and the boundary layer. Recall that, for a long exposure using a large telescope, the half-width of a stellar image β is related to the integral E and the wavelength λ by the expression [8]

$$\beta = 5.31\lambda^{-1/5}E^{3/5}. \quad (2)$$

The methods for estimating the influence of the free atmosphere considered below involve direct determination of the integrated turbulence E_f from stellar scintillations, rather than derivation of the vertical profile of the turbulence.

The scintillation index s^2, which is the dispersion of the natural logarithm of the intensity averaged over the aperture and measured for a fairly short exposure time, is also fully determined by the vertical profile $C_n^2(h)$. It is obviously equal to the dispersion of the flux fluctuations normalized to the mean-square flux. The theory of light propagation in weakly turbulent media (see [8–10] for more details) can be used to calculate s^2 as the integral of the vertical turbulence profile $C_n^2(h)$ with some weighting factor $W(h)$:

$$s^2 = \int_0^\infty C_n^2(h)W(h)dh, \quad (3)$$

where the weighting function is

$$W(h) = 5.21k^2\int_0^\infty f^{8/3}\sin^2(f^2h/2k)A(f)df. \quad (4)$$

Here, $k = 2\pi/\lambda$, f is the modulus of the spatial frequency, and the function $A(f)$ describes the shape of the entrance aperture. For example, for a circular aperture with diameter D, we obtain $A(f) = [2J_1(fD/2)/(fD/2)]^2$, where J_1 is a first-order Bessel function. In the case of non-monochromatic radiation, we must average over the corresponding spectral band, since the weighting function is wavelength-dependent.

Figure 1a presents weighting functions $W(h)$ calculated using (4) for various diameters of our aperture (see Table 1). These functions have been calculated for the V photometric band and the spectral energy distribution of an A0 star. We can see that the dependences in Fig. 1a are close to linear on a logarithmic scale. In the two limiting cases of infinitely small and infinitely large apertures, $W(h)$ is an exact power-law function of the altitude, with indices 5/6 and 2, respectively [8]. For real apertures in the considered altitude interval (from 1 to 20 km), $W(h)$ can be adequately approximated by power laws with indices between 5/6 and 2. An aperture is considered small or large compared to the size of the Fresnel zone, which in our case is about 7 cm. For small apertures, this index is roughly equal to unity, while it is about two for large apertures. It is the substantial difference between the weighting functions for apertures of

Table 1. Characteristics of differential weighting functions

Aperture number	1	2	3	4	7	8	9	0
Physical size, mm	0.30	0.59	1.01	1.52	1.91	2.29	3.32	2.16
Equivalent entrance aperture, cm	1.35	2.66	4.59	6.91	8.68	10.41	15.08	9.82
Approximating exponent α	0.89	0.99	1.16	1.38	1.54	1.67	1.85	1.67

different sizes that makes it possible to estimate the vertical distribution of $C_n^2(h)$.

The variable h in formulas (1), (2), and (3) has the meaning of distance along the line of sight, and coincides with altitude only for measurements at zenith. Scintillation indices or derived parameters obtained at various zenith distances z must be reduced to values at zenith ($z = 0$). This is straightforward, provided the weighting functions have power-law dependences on the altitude and the dependence on the zenith distance can be taken outside the integral. In practice, power-law approximations of the real weighting functions can be used (Table 1). In this case, the error does not exceed 2% for $z < 35°$ for medium-size apertures; for the smallest and the largest apertures, it is much smaller.

The isoplanatic angle of the atmosphere θ_0 describes the size of the field of view of an adaptive telescope [11]. It can also be determined using the integral $C_n^2(h)$, but with the weighting factor $h^{5/3}$:

$$\theta_0^{-5/3} = 2.91k^2\int_0^\infty C_n^2(h)h^{5/3}dh. \quad (5)$$

It was noted some time ago [12] that the weighting function $W(h)$ for a 10-cm aperture is rather close to $h^{5/3}$. Consequently, the scintillation index for this aperture can be used to estimate the isoplanatic angle. The 10-cm aperture with central screening of 0.4, for which the weighting function is closer to $h^{5/3}$, provides even better results. The isoplanatic angle θ_0 at the zenith is calculated using the scintillation index $s_{\rm iso}^2$ measured for such an "isoplanatic" aperture at a zenith distance z:

$$\theta_0 = A'(\sec z)^{8/5}(s_{\rm iso}^2)^{-3/5}, \quad (6)$$

where the coefficient A' is determined from the condition that the proximity of $W(h)$ to an $h^{5/3}$ dependence be uniform in the altitude interval from 1 to 20 km. This relation provides estimates for the isoplanatic angle with accuracy $\pm 2\%$, even for the most unfavorable vertical turbulence distribution. Since θ_0 depends on the wavelength [see (5)], the coefficient A' contains a factor to translate the isoplanatic angle to a wavelength of 500 nm; its values are 0.206, 0.197, and 0.188 for the B, V and R scintillation indices, respectively.

The effective altitude of turbulence, which is naturally defined to be

$$h_{\rm eff} = \int_0^\infty C_n^2(h)hdh/\int_0^\infty C_n^2(h)dh, \quad (7)$$

is a supplementary integrated parameter of the atmospheric turbulence. In addition to being very important for the description of the global properties of a given site, it also provides a relation between the scintillation index in a small aperture, for which the weighting function is roughly proportional to the altitude, and the integral $C_n^2(h)$ over the entire depth of the atmosphere E. Indeed, for such an aperture, $W(h_{\rm eff})h \approx W(h)h_{\rm eff}$, and it follows from (7) that

$$s^2 \approx W(h_{\rm eff})E. \quad (8)$$

The effective altitude of turbulence can also be specified in another way: from the ratio of the scintillation indices for two different apertures, using, for example, a power-law approximation for the weighting functions $W_1(h) \sim h^{\alpha_1}$ and $W_2(h) \sim h^{\alpha_2}$:

$$(h_{\rm eff}^*)^{\alpha_2-\alpha_1} \sim \int_0^\infty C_n^2(h)W_2(h)dh/\int_0^\infty C_n^2(h)W_1(h)dh, \quad (9)$$

where, for the sake of definiteness, $\alpha_2 > \alpha_1$; i.e., the first aperture is smaller then the second.

These two values for the effective altitude of turbulence can differ substantially, depending on the behavior of the function $C_n^2(h)$ in the boundary layer. However, if we consider them only in the free atmosphere by setting a lower integration limit in (7) and (9) above the depth of the boundary layer (≈1 km), these heights become similar. In addition, their difference can be shown to decrease with decrease of $\alpha_2 - \alpha_1$. They coincide with each other and with the geometrical height h, provided there is only one turbulent layer. In any case, $h_{\rm eff}^*$ provides an upper limit for $h_{\rm eff}$.

Figure 1b presents ratios of the weighting functions for various pairs of apertures. Despite the fact that these are equal to the ratios of the corresponding scintillation indices only in the case of a single turbulent layer, the dependences in Fig. 1b can be used to determine the effective altitude in the sense of (9). The easiest way is to use a large and small aperture pair, for which the

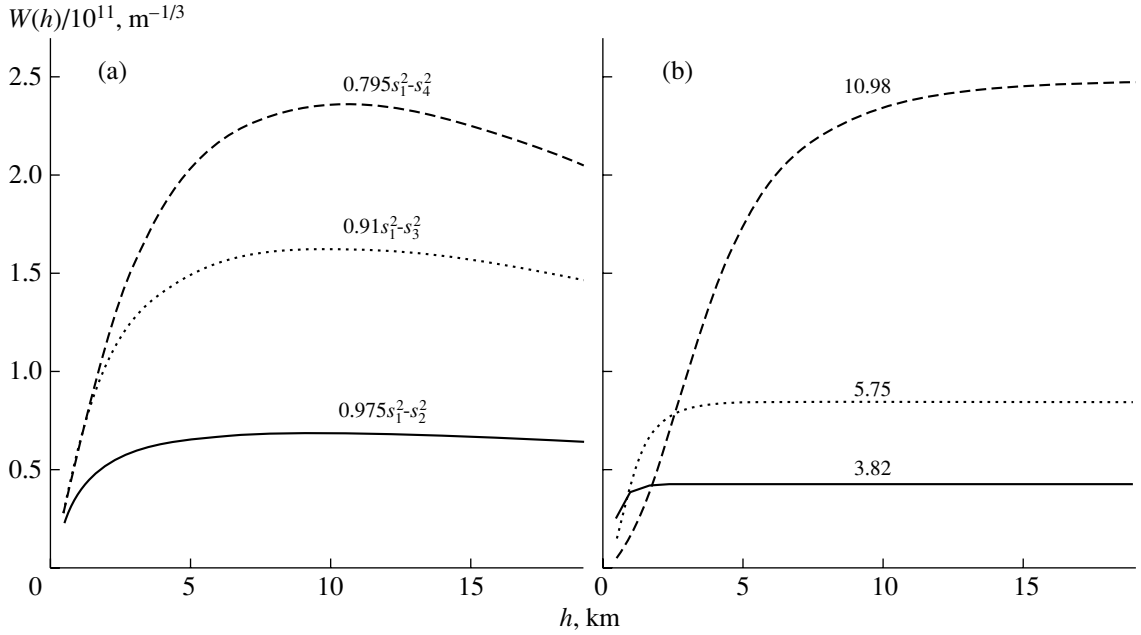

Fig. 2. (a) Differential weighting functions for some pairs of apertures as a function of altitude h. The coefficients were selected so that the functions were constant within the altitude interval considered. (b) Weighting functions for three apertures of the DASS as a function of altitude h. The outer diameters for the apertures in cm are indicated.

ratio of the weighting functions depends on the altitude essentially linearly. This is natural, since the weighting function for a small aperture is roughly proportional to the altitude, while that for a large aperture is proportional to the square of the altitude. In the case of 15.08- and 1.35-cm apertures, for our calculated weighting functions, we obtain the following calibration relation:

$$h^*_{\rm eff} = 80.2(s^2_{15.08}/s^2_{1.35}) - 0.2 \text{ km}. \quad (10a)$$

For 6.91- and 1.35-cm apertures, we obtain in a linear approximation

$$(h^*_{\rm eff})^{0.5} = 5.46(s^2_{6.91}/s^2_{1.35}) + 0.8 \text{ km}, \quad (10b)$$

with accuracy better than 10% (a cubic approximation $(h^*_{\rm eff})^{0.5}$ provides accuracy better than 2%).

Having thus determined $h^*_{\rm eff}$ and assuming that $h_{\rm eff}$ coincides with $h^*_{\rm eff}$ in the free atmosphere, we can derive from (8) the integrated intensity of the turbulence in the free atmosphere $E_f = s^2/W(h^*_{\rm eff})$.

Table 2. Characteristics of DASS apertures and their weighting functions

Apertures	B'	Altitude $h_{0.5}$, km	$W^s/10^{11}$, m$^{-1/3}$	$W_d(3\,\text{km})/W^s$
1–2	0.975	0.84	0.68	0.86
1–3	0.910	1.41	1.60	0.78
1–4	0.795	2.05	2.30	0.66

The uncertainty in this approach is that the altitude of the lower boundary of the free atmosphere is not specified, and depends on the real vertical distribution of the turbulence. Its advantage—stability to noise—is manifest in the case of a large and small aperture pair.

An estimate of the integrated turbulence in the free atmosphere can also be made with another method, using only small apertures. Figure 2a presents simple linear combinations of the weighting functions for pairs of apertures of the form $W_{12}(h) = B'W_1(h) - W_2(h)$. For each pair, coefficient B' is selected so that the difference remains essentially constant (±5%) in the considered altitude interval. Its behavior above 20 km is insignificant. The differential weighting function depends on the sizes of the apertures, and is described by the saturation W^s and altitude $h_{0.5}$ corresponding to 0.5 of the saturation value. The actual values for three pairs of apertures are presented in Table 2.

The differences in the weighting functions correspond to the same differences in the scintillation indices, without any limitations on the vertical distribution of the turbulence. Consequently, the integrated intensity in the free atmosphere (starting approximately from the altitude $h_{0.5}$), for example, for 1.35- and 2.66-cm apertures, is calculated as

$$E_f = (0.975s^2_{1.35} - s^2_{2.66})/W^s_{12}. \quad (11)$$

Although this method yields more definite results than the effective-altitude method, it is obviously more sensitive to noise.

The double-aperture scintillation sensor (DASS) [13] makes it possible to determinate the integrated turbulence in the free atmosphere with even higher accuracy. This technique is based on measurement of the differential scintillation index s_d^2; i.e., the dispersion of the natural logarithm of the ratio of the fluxes I_2 and I_1 for two concentric apertures, one circular and one annular: $s_d^2 = \langle(\Delta \ln(I_1/I_2))^2\rangle$.

The corresponding weighting function $W_d(h)$ is essentially constant starting from some altitude. Figure 2b presents these functions calculated for three of the apertures used. We can see that, compared to the differential weighting functions (Fig. 2a), they initially increase more sharply and are substantially more constant for other altitudes. Table 3 presents the values characterizing these functions indicated above, together with the outer diameters of the apertures.

The integrated turbulence in the free atmosphere is determined from the expression

$$E_f = s_d^2/W^s. \quad (12)$$

The ordinary scintillation indices in each aperture are measured along with the differential scintillation index. The weighting function for a small, central aperture is roughly proportional to the altitude, so that relation (8) for the effective height of the turbulence h_{eff} can be applied.

Using the generalized SCIDAR principle [7], we can also determine the total integral of distortions E over the entire depth of the atmosphere. To this end, it is sufficient to place an annular aperture at some distance from the exit pupil of the telescope, rather than at the pupil, which corresponds to a sort of additional propagation of the light along a turbulence-free path. In other words, the "lens + telescope" optical system will form an image (in this instance, imaginary) of the exit aperture a substantial distance behind the telescope. If the path length exceeds the initial distance interval where the weighting functions increase, the entire atmospheric turbulence falls within the interval with constant weight, which is required to measure the total integral.

The seeing β_{free} determined by distortions in the free atmosphere is a convenient parameter for estimating the contribution of these distortions to the total seeing, generally measured using standard astro-climatic techniques. The seeing reduced to the standard wavelength of 0.5 μm and expressed in arcseconds is calculated using the formula

$$\beta_{\text{free}} = 1.99 \times 10^7 E_f^{3/5}. \quad (13)$$

The exact meanings of E_f, h_{eff}^*, and β_{free} depend on the chosen measurement method, which specifies the corresponding weighting functions. Nonetheless, these quantities are useful for comparative analyses of the roles of the boundary layer and the free atmosphere in astronomical image distortion.

3. INSTRUMENTATION AND TECHNIQUE

Scintillations were measured with a 60-cm Cassegrain telescope (focal length of about 7.5 m) of the Maĭdanak Observatory in 1998 and 1999 using a four-channel *WBVR* photometer. To experimentally verify the ideas presented above, a prototype of a double-aperture scintillation sensor was used during three nights in 1998. In this Section, we will briefly describe these instruments and the observations and data reduction.

A four-channel *WBVR* photometer [14, 15] with beam splitting between the channels provided by dichroic mirrors was chosen for our study of stellar scintillations for the following reasons: (1) it is permanently mounted on the 60-cm telescope and could be used for these measurements over a long period of time; (2) it provides flux detections with accumulation times of 1 ms and shorter; (3) it provides simultaneous flux measurements in the four spectral bands; and (4) it is equipped with a computer-controlled mechanism for rapid changing of the field diaphragms. A detailed optical schematic of the photometer is given in [15].

We modified the four-channel photometer for the stellar scintillation measurements. The focal plane was shifted about 170 mm towards the telescope. In the new focal plane, we mounted a 2-mm field diaphragm (with an angular size of about 1′) and, directly behind it, an additional lens with a focal length of 160 mm, which forms an image of the entrance pupil in the former focal plane. In this way, field diaphragms with a step motor with an accuracy of about 10 μm placed in this plane and on the optical axis become pupil diaphragms (apertures). Since the additional lens was displaced from the optical axis by about 4 mm, the image of the non-obscured segment of the main telescope mirror fell into the pupil diaphragms, and further on the beam-splitting elements. The focal length of this lens was chosen to provide the necessary interval for the effective entrance apertures.

Another additional lens was introduced on the optical axis, together with a wide-field monitoring mirror. Its purpose was to form an enlarged image of the field diaphragm in the focal plane of the eyepiece, in order to center the measured star accurately.

Resetting of the diaphragms is computer controlled, and takes, on average, 0.11 s. Damping of vibrations in the disk after it has stopped lasts another 0.02 s. Table 1 presents the linear sizes of the diaphragms and equivalent entrance apertures. The central screening of the last aperture, used to measure the isoplanatic angle, is 0.4 of its size. The errors in the sizes do not exceed 5% for small and 2% for large diaphragms.

An operational prototype of the Double-Aperture Scintillation Sensor (DASS) was quickly assembled (May–June, 1998) on the basis of the available blocks for the four-channel photometer. The DASS includes only two photomultipliers: one measures the flux I_1 in the annular diaphragm while the other measure the flux I_2 in the inner circular diaphragm.

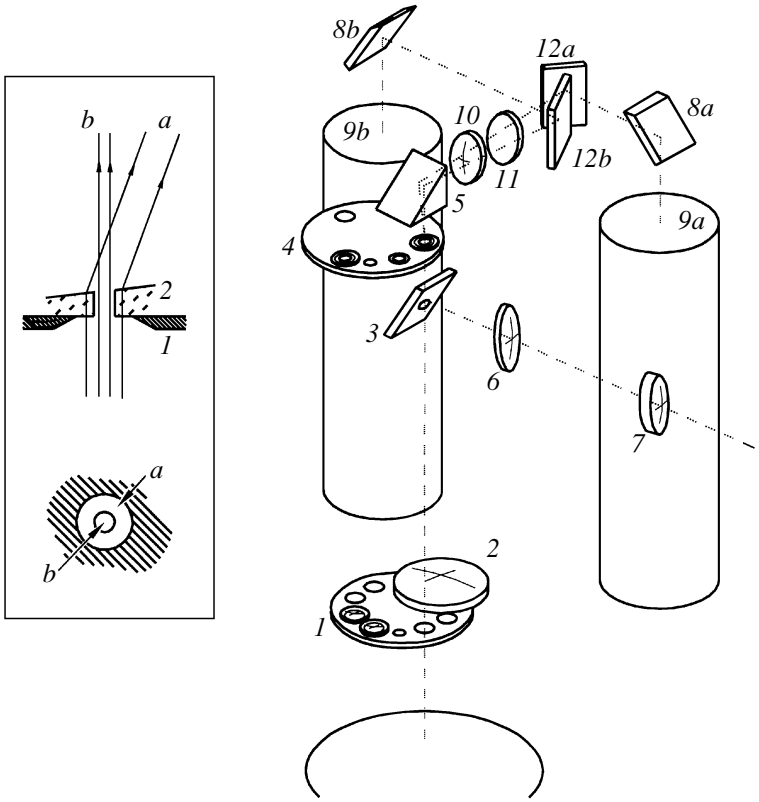

Fig. 3. Simplified optical schematic for the prototype of the differential scintillation sensor. See text for details.

Figure 3 presents a simplified optical schematic for the instrument. The focused light of a star passes through one of the focal diaphragms on disk *1* and lens *2* with focal length 160 mm. The image of the pupil is formed on a second disk with exchangeable diaphragms *4*, three of which contain microprisms with a central hole, which determine the parameters of the double aperture. As shown in the inlay in Fig. 3, the central portion of beam *b* passes through the hole without deviation, while the annular zone *a* is deflected slightly by the microprism. Both beams are deflected by the auxiliary prism *5*, and lens *10* again forms an image of the focal plane near the splitting mirrors *12a* and *12b*; a *V*-band filter *11* is located in front of these.

In this way, the annular and central apertures form two separate images of the entrance diaphragm near mirror *12ab*. Further, both beams are deflected by mirrors *8a* and *8b* toward the photocathodes of photomultipliers *9a* and *9b*, which measure the fluxes in the annular and inner circular apertures. To measure the isoplanatic angle, there is a diaphragm with central screening 0.4 in disk *4*, similar to that in the four-channel photometer. Naturally, in this case, light falls on only one photomultiplier.

Only part of the image of the telescope pupil passes through the hole in mirror *3*; the remainder serves as an observation of the image of the star, which is formed by lens *6* with eyepiece *7* for the purpose of guiding.

We used three double apertures of different sizes with the ratio of the inner to the outer diameters equal to 0.5. Table 3 presents the outer diameters of the annular apertures projected onto the entrance pupil of the telescope, together with the parameters of the corresponding weighting functions.

Two diaphragms with positive lenses are available for the realization of the generalized SCIDAR mode in the disk with the focal diaphragms. The focal lengths of these lenses are 30 and 15 mm, which corresponds to "shifts" of the entrance aperture to –2 and –4 km. In this case, the weighting functions corresponding to diaphragms *1* and *3* are already close to saturation (Fig. 2b), and the measurements correspond to the integrated effect of the entire atmosphere. However, the total range of sight measured in this way was between 1″ and 1″.5, which is systematically higher than simultaneous DIMM and

Table 3. Characteristics of the photometer aperture set

Apertures	Diameter, cm	Altitude $h_{0.5}$, km	$W^s/10^{11}$, $m^{-1/3}$	$W_d(3\,km)/W^s$
1	3.82	0.4	0.43	1.00
2	10.98	3.5	2.45	0.41
3	5.75	1.0	0.85	0.91

GSM estimates. The reason for these discrepancies is probably the presence of strong dome turbulence. Intense and slow distortions were seen on the 60-cm telescope with a Foucault blade. Similar effects also occurred on the 1.5-m telescope; in both cases, the seeing improved toward the morning. We will not consider the results of the integrated seeing measurements obtained with the DASS prototype further here.

The real-time detection of the signal and reduction of the measurements were essentially the same for the DASS and four-channel photometer. Both instruments work in a photon-counting regime and have the same type of high-speed impulse amplifiers. We used electronic instrumentation from the four-channel photometer for the DASS, in particular, counters with a response rate of 100 MHz in a specially-designed interface in a personal computer.

The duration of an individual signal accumulation (microexposure) obviously affects the measured scintillation index, since the power of the flux fluctuations is partially lost on timescales shorter than the accumulation time. Figure 4 presents the results of specialized measurements with various accumulation times for diaphragm *3* of the DASS (equivalent entrance aperture 5.75 cm). We can see that, for 1-ms microexposures, the loss for the central and annular apertures does not exceed 0.03, and is ≈0.1 for the differential scintillation index. This is due to the fact that low-frequency fluctuations are suppressed in the differential signal. On the other hand, if a microexposure is too short, the statistical noise dominates in the signal, even for bright stars, and the corresponding errors can also distort the measured values. In our opinion, microexposures of 1 ms (0.99 ms for accumulation, 0.01 ms for a pause between microexposures) represent a reasonable compromise.

A correction for the finite accumulation time can be found by extrapolating the indices obtained with 1-ms and 2-ms accumulations. In this case, a series with 2-ms microexposures is formed from two-element combinations (binning) of the initial 1-ms series. We plan to apply this procedure in future scintillation measurements.

For the measurements with the photometer and double-aperture scintillation sensor, we used a slightly modified version of the standard OPERA-VI code, which controls the photometer and measurement process during ordinary photometric observations. A program block was added to calculate the required statistical parameters of the light flux and (during operation of the four-channel photometer) periodically change the aperture diaphragms.

Let us first consider a measurement cycle with the photometer. We measured the scintillation indices quasi-simultaneously in eight (six, in 1999) apertures and in the *B*, *V* and *R* channels. The data from the *W* channel were not used due to their insufficient statistical accuracy, even for bright stars. In our case, "quasi-simultaneous" means that the cycle of consecutive estimations of the scintillation indices in all three apertures

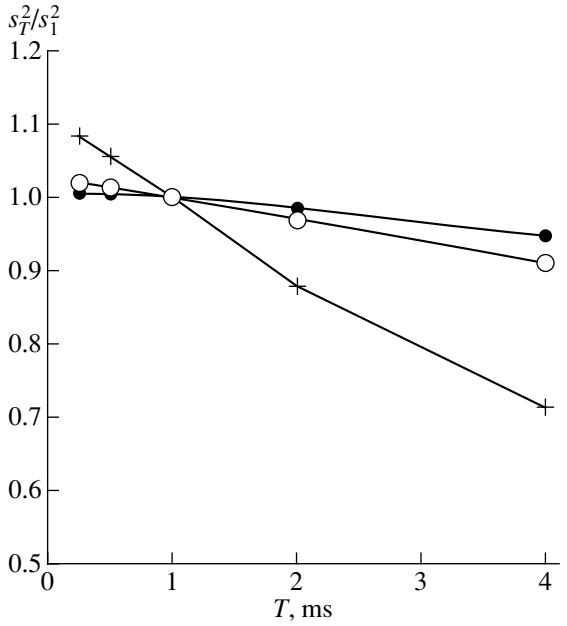

Fig. 4. Detected intensity as a function of accumulation time *T*, normalized to the intensity for a 1-ms accumulation. The measurements were made with the DASS and aperture 3. The crosses show the differential index, the circles the central index, and the dots the scintillation index for the annular aperture.

was much shorter than the time to complete an individual measurement of these values. The time for a complete measurement is limited from above by the characteristic time over which scintillation can be considered a steady-state process. On the other hand, replacement of an aperture should not occupy a considerable fraction of the total time, which imposes restrictions on the minimum time for estimation of the indices with the current aperture.

Based on these considerations, we chose to use a measurement cycle in which 1000 counts with 1-ms exposures were accumulated with each aperture. About 15% of the total time was lost due to aperture switching. A series of measurements with all eight apertures takes roughly 9 s. This series is repeated 26 times (33 times for the measurements with six apertures), so that the total time to obtain one estimate of the scintillation indices is 4 min. The total time for measurements with the scintillation sensor was usually 50 s.

The real-time reduction procedure for the measurements consisted of the following.

(1) For a series of 1000 counts obtained simultaneously in the three channels, we calculated the mean $\bar{n}'_B$, $\bar{n}'_V$, and $\bar{n}'_R$ values; dispersions $\sigma_B^{2'}$, $\sigma_V^{2'}$, and $\sigma_R^{2'}$; and covariances cov'_{BV}, cov'_{BR}, and cov'_{VR} in the usual way (for the DASS measurements, $\bar{n}'_1$, $\bar{n}'_2$, $\sigma_1^{2'}$, $\sigma_2^{2'}$, and cov'_{12} were calculated).

(2) We corrected the calculated statistical parameters for the non-linearity of the detectors, which is essential for measurements with large entrance apertures (for aperture 9 of the photometer and the star α Lyr, the flux of impulses reached 2×10^6 pulse/s). In a linear approximation, which works well for fluxes below $\sim 3 \times 10^6$ pulse/s, we determined the true means and second moments from the formulas

$$\begin{aligned} \bar{n}_i &= \bar{n}_i'(1 + \bar{n}_i'\tau_i), \\ \sigma_i^2 &= \sigma_i^{2'}/(1 - 2\bar{n}_i'\tau_i)^2, \\ \mathrm{cov}_{ij} &= \mathrm{cov}_{ij}'/((1 - 2\bar{n}_i'\tau_i)(1 - 2\bar{n}_j'\tau_j)), \end{aligned} \tag{14}$$

where a prime denotes values obtained in step 1 and τ is a non-linearity parameter specific to each photometric channel.

(3) Next, we determine the statistical parameters of the scintillations—the indices s_B^2, s_V^2, and s_R^2 and the differential indices s_{BV}^2, s_{BR}^2, and s_{VR}^2 (for the DASS measurements, s_1^2, s_2^2, and s_d^2)—using the relations

$$\begin{aligned} s_i^2 &= (\sigma_i^2 - p_i\bar{n}_i)/(\bar{n}_i - \bar{b}_i)^2, \\ s_{i-j}^2 &= s_i^2 + s_j^2 - 2\mathrm{cov}_{ij}/((\bar{n}_i - \bar{b}_i)(\bar{n}_i - \bar{b}_i)), \end{aligned} \tag{15}$$

where *i* and *j* are the *B*, *V* and *R* channels for the photometer and *1* or *2* for the scintillation sensor. The quantity $\bar{b}_i$ is the sky background in a given channel, and p_i is the so-called non-Poisson coefficient, which is close to unity.

(4) The resulting values were summed (six indices and three means for each of eight or six apertures for the measurements with the four-channel photometer, or three indices and two means for measurements with the DASS). At the end of the entire process, averages with their rms errors were calculated, displayed on a monitor, and stored in a data file.

Since the average was used for each 1 s estimate of the second moments, this rather effectively filtered out the influence of slow variations of the signal due to the motion of the star in the field diaphragm (which was 1′ for the telescope used), low-frequency scintillations, and variations in opacity. Since the real sky background is much lower than the flux from the stars, even on moonlit nights, a crude estimate for this background can be used in (15).

We can see from (14) and (15) that the resulting scintillation indices are affected by two instrumental parameters for each photometric channel. The first, τ, must be determined with a relative accuracy of ≈0.1 if we wish to achieve a ≈3% accuracy in the indices for measurements at the maximum fluxes. The non-linearity of photometric channels for both instruments was periodically studied using a method based on the influence of the non-linearity on the measured statistical parameters of Poisson-type fluxes [16]. The slope of the dependence between the ratio $p = \sigma^2/\bar{n}$ and the flux is related to the non-linearity parameter τ (sometimes called the dead time). This method estimates the non-linearity parameter with an accuracy better than 5%. Within these limits, τ is constant and, depending on the channel, equal to 28–31 ns. The impact of τ on measurements of indices with small apertures is obviously negligible.

The same auxiliary measurements make it possible to determine the second parameter, the non-Poisson coefficient *p* for small fluxes. Ideally, this should be unity; in reality, however, it differs slightly from unity for a number of reasons (after-pulses of the photomultiplier, "ringing," noise pick-up, etc.). It follows from (15) that the error Δ*p* gives rise to an error in the scintillation index $\Delta p/\bar{n}$, and correct reduction of the measurements for small fluxes (with diaphragms *1* and *2*) requires that the accuracy in *p* be no worse than 0.01. For example, the coefficients *p* determined from measurements in July 1998 in the *B*, *V*, and *R* channels were 0.997, 0.994, and 1.002, respectively, with the error Δ*p* roughly equal to 0.003. We determined the parameters of the photometric channels in each season of stellar scintillation measurements. In addition, we verified the correctness of the instrumentation and data reduction using measurements of a constant light source (light-emitting diode) with a flux corresponding to the stellar fluxes. We also measured the extremely weak scintillation displayed by Jupiter.

Based on the above considerations, we used bright stars: α Lyr, α Cyg, α And, and α Aur. For the faintest of these, α And, $V = 2\overset{m}{.}05$. The data indicate that, for this star, there begins to be a deficit of light in the smallest aperture. However, since the weighting functions and, accordingly, the scintillation indices are only weakly sensitive to variations of the spectral band, we can move $\approx 0\overset{m}{.}5$ toward fainter stars by removing the photometric filters from the photometric channels [15].

4. RESULTS

General information. A complete summary of the scintillation measurements made with the instrumentation described here is presented in INTAS Reports [17, 18]; electronic versions can be obtained from the authors. Table 4 presents the general statistical data for the measurements that have been made thus far. The following data are presented for each series of observations: the dates of the beginning and end of the measurements, the total duration of the measurements in hours, the number of complete measurements (separately for the DASS, and with the number of isoplanatic-angle measurements in brackets), the instrument used, and the observers.

We stress again that our observations with the DASS prototype were carried out to verify the new technique for measuring the seeing, while the observations with the four-channel photometer were intended for a long-

Table 4. General information about the scintillation measurements

Season	Beginning and end dates	Number of hours	Number of measurements	Instrument	Observers
1	July 17–19, 1998	19	183(409)	DASS	O. Vozyakova, V. Kornilov, A. Tokovinin
	July 20–25, 1998	30	377	Photometer	
2	July 24–August 8, 1999	97	1288	Photometer	O. Vozyakova, V. Kornilov
3	September 26–October 12, 1999	132	1765	Photometer	S. Il'yasov, T. Sadibekova

term study of the scintillations aimed at obtaining supplementary data on the atmospheric turbulence at Maĭdanak.

The 1998 measurements were carried out with the complete set of apertures. Our analysis indicates that apertures 7 and 8 (Table 3) can be excluded from further measurements. Figure 1a also confirms that these apertures essentially reproduce the measurements with the "isoplanatic" aperture.

Table 5 presents characteristic values for the scintillation indices and their relative errors calculated assuming that consecutive estimates are statistically independent. These values are medians of the distributions for four-minute measurements of α Cyg in the *V* channel obtained during season 2. The data presented show that the measurement errors are determined primarily by the scintillation process rather than by quantum statistics.

We used the *V*-channel scintillation indices for further analysis, while the data in the *B* and *R* channels were used to check the results. Further, we plan to use the entire data set to reconstruct the vertical distribution of the turbulence.

Isoplanatic angle. Figure 5 presents a histogram of all estimates of the isoplanatic angle derived from the scintillation indices in the "isoplanatic" aperture in the *V* band. The θ_0 values determined from the *B*, *V*, and *R* data coincide to better than 2%. In addition, an appreciable part of the small deviations can be explained as a result of the effective height of the turbulent layer, providing evidence for the reliability of our measurements and the validity of the theoretical models used. Table 6 presents numerical values for the levels of the cumulative distribution θ_0.

The median isoplanatic angle is $2\farcs30$, which is typical for good observatory sites. For example, the study [19] gives isoplanatic angles from $1\farcs3$ to $3\farcs0$ for Mauna Kea; the few available data on vertical atmospheric sounding above Paranal yield $\theta_0 = 3\farcs0$ [4]. Season-to-season variations are small, and the cumulative distributions for the isoplanatic-angle estimates are similar to each other. These are the first such data to be obtained for Maĭdanak.

The effective altitude of the turbulence and the integrated turbulence in the free atmosphere are related via the scintillation index in a small aperture, as shown in Section 2. Therefore, these parameters were determined simultaneously both from the ratio of the scintillation indices for large and small apertures ($h^*_{\rm eff}$) and from differences in the indices for small apertures ($h_{\rm eff}$). Figure 6a presents a comparison between the altitude $h^*_{\rm eff}$ calculated from the ratio of the indices for the 1.35- and 6.91-cm apertures [see (10b), cubic approximation] and $h_{\rm eff}$, obtained from (8) using estimates for the integrated turbulence E_f. Here, E_f is determined from the difference of the indices for 1.35- and 4.59-cm apertures [see (11)].

The average behavior of this dependence can be understood as follows: (1) below 4 km, the differential method underestimates the integrated turbulence and, hence, overestimates $h_{\rm eff}$; (2) from 4 to 10 km, there are usually two (or more) turbulent layers present, which results in overestimation of the altitude $h^*_{\rm eff}$; (3) above 10 km, only turbulence in the tropopause is important, and the two heights coincide; (4) $h_{\rm eff}$ values are overestimated above 12 km due to their appreciably non-normal error distribution (the difference of the indices is of the order of the errors). Similar dependences are found when the effective heights are determined from measurements in other apertures.

The errors in the effective heights were estimated based on the measured errors for the scintillation indices and formulas (8), (11), and (10). Typical relative errors for $h^*_{\rm eff}$ are 0.04 and 0.06 using (10a) and (10b), respectively. The relative errors do not depend on altitude. The relative errors in $h_{\rm eff}$ increase with altitude, and their characteristic values at 10 km are 0.20, 0.13, and 0.11 for the index differences (1–2), (1–3), and (1–4), respectively. In this case, the absolute errors increase faster than the altitude (roughly as $h^{1.5}$), as can be seen in Fig. 6a. Taking this into account, we will specify the effective height $h^*_{\rm eff}$ based on the index ratio $s^2_{6.91}/s^2_{1.35}$ (10b).

Table 5. Characteristic scintillation indices and their relative errors

Aperture number	1	2	3	4	0	9
Scintillation indices	0.108	0.091	0.064	0.041	0.021	0.011
Relative errors	0.05	0.04	0.04	0.04	0.04	0.04

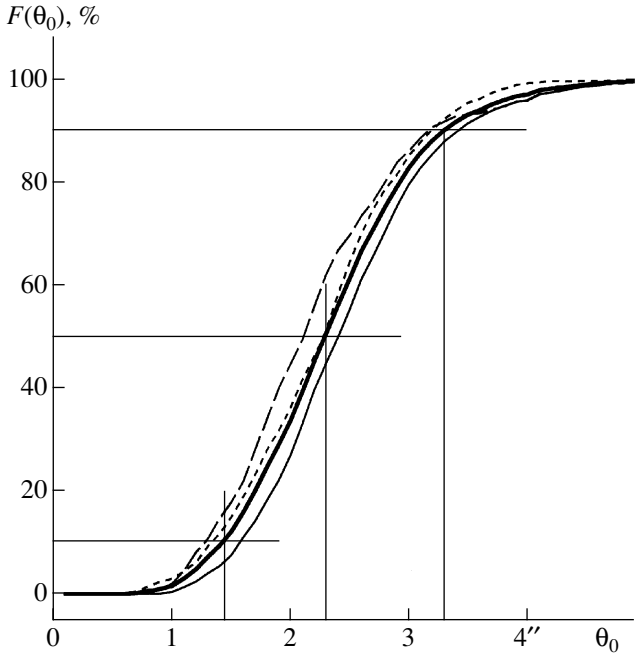

Fig. 5. Cumulative distribution for the isoplanatic angles for three measurement seasons (summer 1998—long dashes; summer 1999—short dashes; autumn 1999—thin solid curve) and their integrated distribution (thick solid curve).

Figure 6b presents distributions for $h^*_{\rm eff}$ for three measurement seasons. The distributions for seasons 2 and 3 are appreciably different: in season 2, effective heights from 3 to 6 km dominated, while the dominant effective heights in season 3 were from 6 to 10 km. It appears that, in the latter case, there was usually a single turbulent layer in the tropopause, whereas, in the former case, an additional low layer of intense turbulence dominated. The altitude distribution for season 1 includes both features. Note that the first two seasons fell in periods of unstable weather conditions associated with passing atmospheric fronts. The third season (autumn 1999) was characterized by stable, good weather.

Analyzing the measurements for individual nights, we can see that, as a rule, the effective height of the turbulent layer sharply decreased during characteristic bursts of scintillations lasting 15–30 min. This provides evidence for the passage of a low layer (area) of increased turbulence several kilometers in size across the line of sight.

Table 6. Characteristics of cumulative distribution for isoplanatic angle

Levels	Season 1	Season 2	Season 3	All measurements
$F(\theta_0) = 10\%$	1.″29	1.″33	1.″57	1.″44
$F(\theta_0) = 50\%$	2.12	2.28	2.40	2.30
$F(\theta_0) = 90\%$	3.19	3.20	3.43	3.32

The integrated turbulence in the free atmosphere E_f is presented below as the contribution of the free atmosphere to the seeing (the half-width of the turbulent image of a star in a large telescope) $\beta_{\rm free}$ [see (13)]. We determined the seeing from both our DASS and photometer measurements. It follows from Section 2 that the DASS provides the most reliable seeing estimates; however, the small number of measurements with the DASS prototype prevented a complete statistical analysis of the data.

Figure 7 presents a comparison between the seeing for the entire atmosphere (estimated using GSM and DIMM data) and the contribution of the free atmosphere $\beta_{\rm free}$ (estimated using the DASS data for two of three observational nights when this instrument was used). On July 18, we used apertures 1 and 2, while aperture 3 was used on July 19; strictly speaking, the meanings of $\beta_{\rm free}$ for these three apertures are somewhat different. However, a comparison between the results obtained with the different apertures shows that they are virtually indistinguishable. The effective height of the turbulence on July 18 was, on average, 7–8 km, while it was 4–5 km on July 19; i.e., in all cases, the turbulent layers were in the area of saturation for the weighting functions of the corresponding apertures (Fig. 2b).

Figure 7 also show a good agreement between the estimates of the total β obtained with different astro-climatic instruments. On July 18, when the seeing was close to its median value, the dominant contribution was made by the boundary layer. On July 19, when the image quality was better, the situation was similar; toward morning, however, the turbulence in the free atmosphere increased and the image quality deteriorated.

As a more dramatic example, Fig. 7 presents data for two nights of season 1 (photometer measurements). The denser series of estimates of $\beta_{\rm free}$ clearly indicate that, on these nights, not only did the total seeing vary substantially during a single night, but the contribution of the free atmosphere also varied from ≈15% (July 23, $18^{\rm h}$ – $19^{\rm h}$ UT) to ≈60% (during the bursts of July 22 around $17^{\rm h}$, $18^{\rm h}30^{\rm m}$, and $22^{\rm h}$ UT).

For the photometer data, we determined $\beta_{\rm free}$ using two methods, as was done for the effective heights: using the effective height $h^*_{\rm eff}$ (10b) and formula (8) (further, we denote this value $\beta^*_{\rm free}$), and using differences of scintillation indices in small apertures (11). The resulting E_f were then transformed into the seeing using (13).

We estimated the errors in $\beta_{\rm free}$ in the same way as those for the effective heights. For example, the relative errors in $\beta^*_{\rm free}$ are essentially independent of this parameter; their median value is 0.032. Accordingly, the absolute

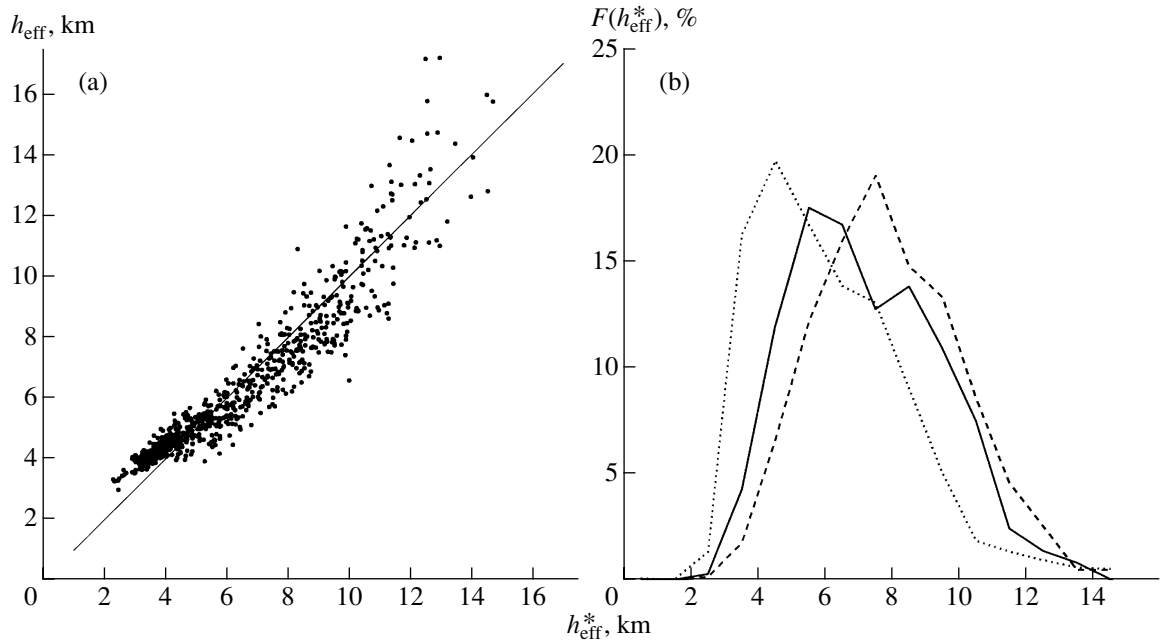

Fig. 6. (a) Relation between the altitudes h^*_{eff} calculated using formula (10b) and h_{eff} derived from the difference of the indices for 1.35- and 4.59-cm apertures using (11) and (8), from the data for seven selected nights. The line corresponding to coincidence of the altitudes is indicated. (b) Frequency distribution of the effective heights h^*_{eff} for three measurement seasons (summer 1998—solid curve; summer 1999—dotted curve; autumn 1999—dashed curve).

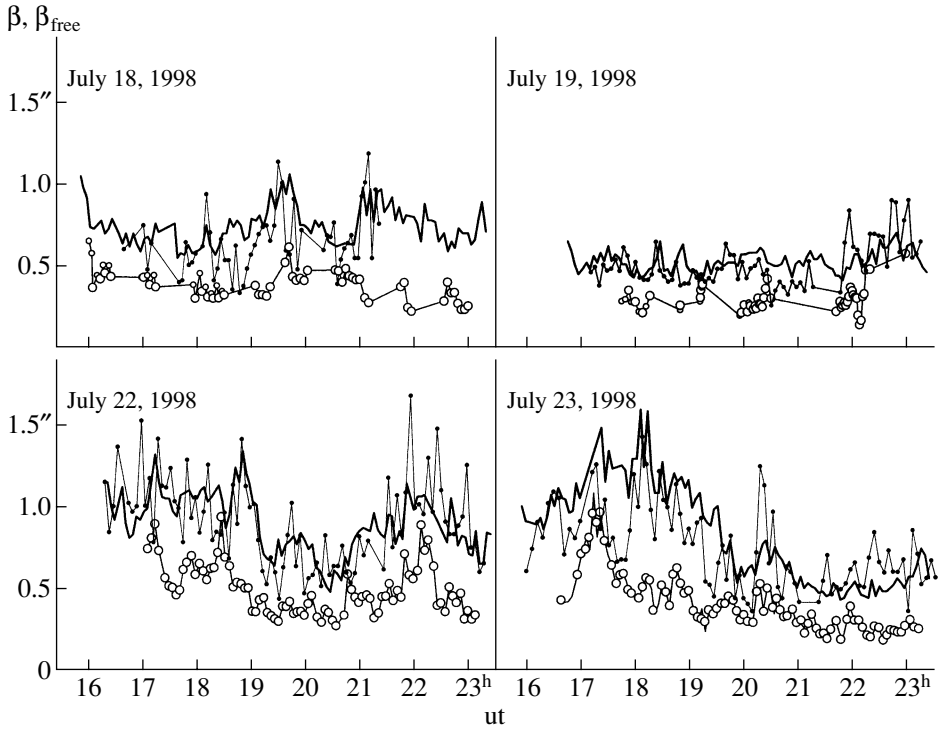

Fig. 7. Evolution of free-atmosphere contribution to seeing β_{free} (circles with curve) during the nights of July 18 and 19, 1998, for measurements with the DASS prototype, and during the nights of July 22 and 23, 1998, for measurements with the photometer. The β_{free} values for the photometer were calculated from the ratios $s^2_{6.91}/s^2_{1.35}$. For comparison, the total seeing β derived from GSM (curve) and DIMM (dots with curve) measurements is plotted.

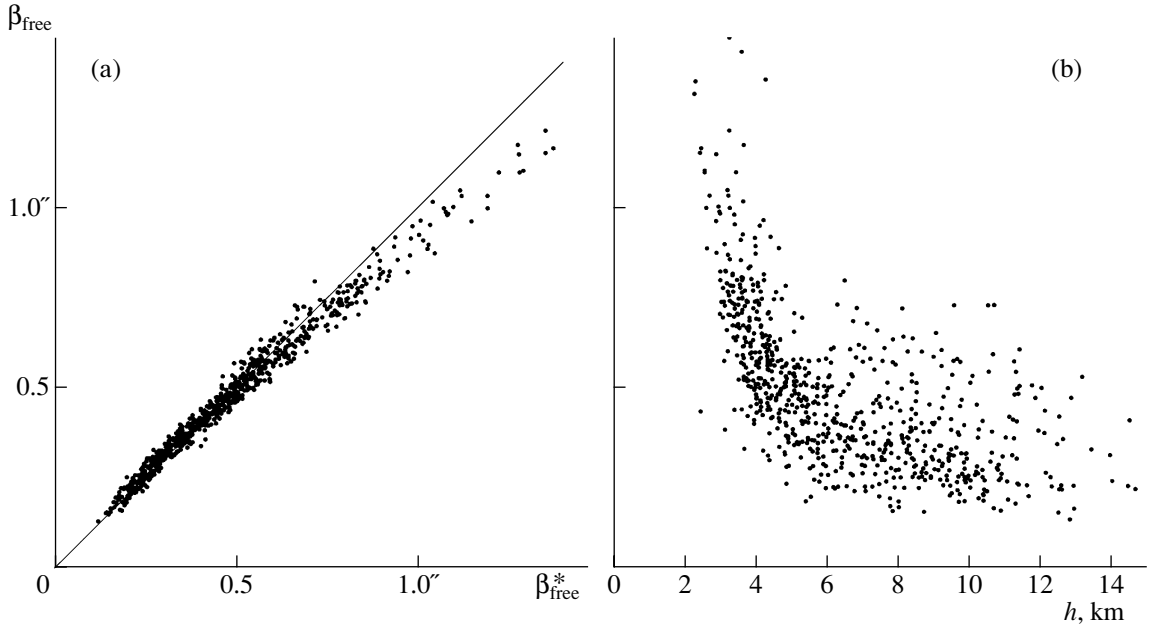

Fig. 8. (a) Comparison of β_{free} obtained from differences of the scintillation indices in apertures 1 and 3 and β^*_{free} derived from the effective height h^*_{eff} and (b) dependence of β_{free} on the effective height h^*_{eff} for seven selected nights. The curve $\beta^*_{free} = \beta_{free}$ is indicated.

errors are nearly proportional to β^*_{free} (for $\beta^*_{free} = 0\farcs3$, they are $\approx 0\farcs01$). For the β_{free} values derived from differences of the scintillation indices, another situation is realized. The absolute errors in this parameter are virtually independent of its value, and their median values are $0\farcs035$, $0\farcs022$, and $0\farcs019$ for the index differences (1–2), (1–3), and (1–4), respectively.

Figure 8a presents a comparison between β^*_{free} and β_{free}, calculated from the difference of the scintillation indices in apertures 1 and 3. We can see that the agreement is good for small values of β_{free}, while β_{free} is systematically less than β^*_{free} when $\beta_{free} > 0\farcs5$. This can be understood as a consequence of the fact that, as a rule, large values of β_{free} occur for low altitudes of the dominating turbulence (Fig. 8b), where the contribution of the turbulence in E_f is underestimated (see the weighting function for the pair 1–3 in Fig. 2a). When the pair 1–2 is used, the analogous relation indicates better average agreement; however, the scatter of the points is appreciably larger. The situation is opposite for the pair 1–4.

Table 7. Characteristics of cumulative distribution for β_{free} and R_{free}

Levels	Season 1	Season 2	Season 3	All measurements
$F(\beta_{free}) = 10\%$	$0\farcs29$	$0\farcs32$	$0\farcs22$	$0\farcs25$
$F(\beta_{free}) = 50\%$	0.43	0.49	0.34	0.39
$F(\beta_{free}) = 90\%$	0.68	0.87	0.52	0.72
$F(R_{free}) = 10\%$	0.26	0.29	0.19	0.22
$F(R_{free}) = 50\%$	0.41	0.45	0.34	0.38
$F(R_{free}) = 90\%$	0.74	0.67	0.50	0.58

We used the parameter β^*_{free} for statistical studies of the contribution of the free atmosphere to the total image distortion. Figure 9a presents individual cumulative distributions for three seasons together with the total cumulative distribution. Table 7 presents numerical levels for these distributions. The distributions for β_{free} (derived from the difference between apertures 1 and 3) differ only in the area of "poor" images, as follows from the above considerations.

The median value for β^*_{free} for all three seasons is $0\farcs39$. Comparing this value to the median seeing for Maĭdanak, which is $0\farcs70$ [3], indicates the relative contribution R_{free} of the free atmosphere to be 37%. This estimate can be refined using the simultaneously made DIMM measurements.

Since the scintillation and DIMM measurements were not synchronized, the instruments were located at different points of the Maĭdanak Observatory and different stars were used for each set of measurements; the hourly-averaged values of β^*_{free} and β were compared. Figure 9b presents distributions for R_{free}, and Table 7

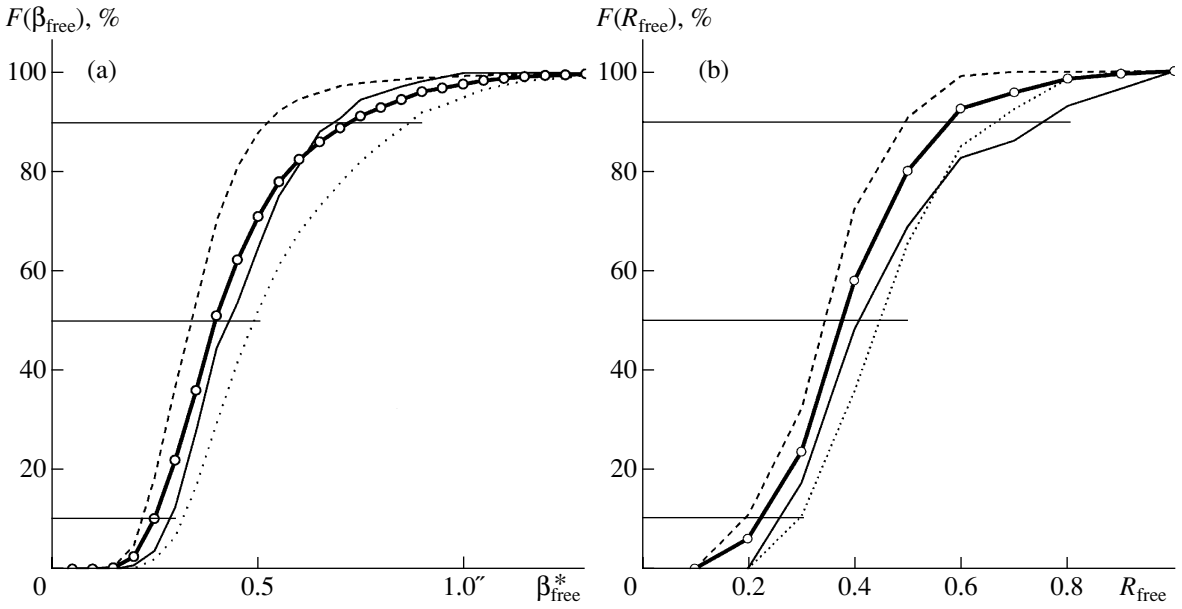

Fig. 9. Cumulative distributions $F(\beta)$ of (a) the free-atmosphere contribution to the image β^*_{free} and (b) the relative contribution R_{free} for three measurement season (summer 1998—solid curve; summer 1999—dotted curve; autumn 1999—dashed curve) and the total cumulative distribution (circles with thick curve). The 10, 50, and 90% levels are indicated.

the numerical parameters for these distributions. The median value for all the estimates is 38%. We can see that, in the best season (autumn 1999), the relative contribution of R_{free} is systematically smaller (34%), while the opposite is true in the worst season (summer 1999, 45%). This also provides evidence that the main reason for deterioration of the seeing is the state of the free atmosphere. Note also that the correlation between the integrated turbulence in the boundary layer E_b and that in the free atmosphere E_f estimated from the same data is relatively small, and equal to 0.3 to 0.5, depending on the season.

Our simplified model of the free atmosphere above Mt. Maĭdanak is based on two assumptions. In the case of minimum observed turbulence, all the free atmosphere is concentrated in the tropopause at a height of 10 km above the mountain (Fig. 6b). The intensity and altitude of this layer are constant. Increases in the integrated turbulence are due to the appearance of an additional layer at a height of 3 km. As noted above, this can clearly be seen when the effective heights and integrated turbulences for individual nights are compared. The fact that this layer is isolated from the turbulence boundary layer is confirmed by the low correlation between E_b and E_f estimated above.

The only free parameter in this model is the ratio of the integrated turbulence in the lower and upper layers E_L/E_H. The relations presented in Figs. 6a, 8a, and 8b, as well as the relation between the E_f values derived using (11) for aperture pairs (1–3) and (1–4), impose restrictions on the heights of both the upper and lower layers. The model dependences between β^*_{free}, β_{free}, h^*_{eff}, and h_{eff} are completely consistent with the observed relations plotted in the corresponding figures. The entire observed ranges of these values can be provided by variations of the free model parameter from 0 to ≈50 for $E_H = 10^{-13}$ m$^{1/3}$.

This simplified, mean-statistical model apparently reflects the regional role of the Pamirs massif, located to the east from Mt. Maĭdanak and having a characteristic height of about 6 km above sea level.

5. CONCLUSIONS

The first thing we would like to stress is the real possibility of determining supplementary integrated parameters describing turbulence in the free atmosphere (at altitudes from 1 to 20 km) on the basis of relatively simple measurements of stellar scintillations. These parameters include the isoplanatic angle θ_0, the effective height of the turbulence h_{eff}, and the integrated turbulence in the free atmosphere E_f or its contribution to the seeing β_{free}.

The most accurate values for these parameters can be derived using the differential-scintillation method. Full realization of the double-aperture scintillation sensor will undoubtedly make it possible to obtain much more information about turbulence in the Earth's atmosphere than is provided by the prototype we tested with these observations. However, an ordinary photoelectric photometer with the ability to detect fluxes on timescales of about 1 ms and at least two rapidly switching apertures is also able to provide fairly reliable data on

turbulence in the free atmosphere. The fact that even using only part of the data yielded a clear picture of the turbulence structure provides hope for a mathematically correct determination of the $C_n^2(h)$ profile via solution of the inverse problem.

Another important conclusion concerns the astroclimate of the Maĭdanak Observatory. This site features not only good median seeing, but also relatively weak turbulence in the free atmosphere, as indicated by its rather large median isoplanatic angle.

A comparison of the total seeing obtained using traditional methods and our estimates for the free atmosphere contribution to the seeing indicates that, as a rule, the contribution of the free atmosphere does not dominate. As is true of many other contemporary observatories, a considerable fraction of distortions (on average, around 60%) originates in the boundary layer immediately above the summit. However, the role of the free atmosphere increases when the images degrade. Periods of appreciable amplification of the turbulence in the free atmosphere can be reliably identified with the appearance of a low, intense, turbulent layer at a height of about 3 km.

ACKNOWLEDGMENTS

This study was partially supported by INTAS (grant INTAS-96-0367). We are grateful to our colleagues from the Sternberg Institute and Tashkent Astronomical Institute O. Vozyakova, S. Il'yasov, and T. Sadibekova, who carried out a substantial fraction of the observations, Yu. Tillaev and Kh. Sultanov, who kindly presented data from their DIMM observations; and A. Aliev, S. Ponomarenko, and A. Zaĭtsev, who helped with some technical problems.

REFERENCES

1. F. Martin, A. Tokovinin, A. Ziad, *et al.*, Astron. Astrophys. **336**, L49 (1998).
2. P. V. Shcheglov, *Problems in Optical Astronomy* [in Russian] (Nauka, Moscow, 1980).
3. S. P. Il'yasov, A. K. Baĭdzhumanov, M. Sarazin, *et al.*, Pis'ma Astron. Zh. **25**, 156 (1999) [Astron. Lett. **25**, 122 (1999)].
4. M. Sarazin, http://www.eso.org/gen-fac/pubs/astclim/paranal.
5. C. Munoz-Tunon, J. Vernin, and A. M. Varela, Astron. Astrophys., Suppl. Ser. **125**, 183 (1997).
6. A. Ziad, R. Conan, A. Tokovinin, *et al.*, Appl. Opt. (2000) (in press).
7. R. Avila, J. Vernin, and E. Masciadri, Appl. Opt. **36**, 7898 (1997).
8. F. Roddier, in *Progress in Optics*, Ed. by E. Wolf (North-Holland, Amsterdam, 1981), Vol. 19, p. 281.
9. V. I. Tatarskiĭ, *Wave Propagation in a Turbulent Medium* (Nauka, Moscow, 1967; McGraw-Hill, New York, 1961).
10. J. Krause-Polstroff, E. A. Murphy, and D. L. Walters, Appl. Opt. **32**, 4051 (1993).
11. D. L. Fried, J. Opt. Soc. Am. **72**, 52 (1982).
12. G. Loos and C. Hogge, Appl. Opt. **18**, 2654 (1979).
13. A. A. Tokovinin, Pis'ma Astron. Zh. **24**, 768 (1998) [Astron. Lett. **24**, 662 (1998)].
14. V. G. Kornilov and A. V. Krylov, Astron. Zh. **67**, 173 (1990) [Sov. Astron. **34**, 90 (1990)].
15. V. G. Kornilov, Balt. Astron. **7**, 513 (1998).
16. V. G. Kornilov and T. M. Pogrosheva, Astron. Zh. **66**, 424 (1989) [Sov. Astron. **33**, 213 (1989)].
17. A. Tokovinin, V. Kornilov, R. Conan, *et al.*, INTAS 96-0367 Progress Report, 1998, No. 1, Part II.
18. V. Kornilov, A. Tokovinin, O. Vozyakova, *et al.*, INTAS 96-0367 Final Report, 1999, No. 2, Part III.
19. D. G. Sandler, S. Stahl, J. R. P. Angel, *et al.*, J. Opt. Soc. Am. A **11**, 925 (1994).

Translated by K. Maslennikov